Late Pleistocene – Holocene denudation, uplift, and morphology evolution of the Armorican Massif (western Europe)

Oswald V. Malcles[1], Stéphane Mazzotti[1], Philippe Vernant[1], Vincent Godard[2]

5   *1. Géosciences Montpellier, Université de Montpellier, CNRS*

2. CEREGE, Aix Marseille Univ., CNRS, IRD, INRA, Coll. France

Correspondence to: Oswald V. Malcles (oswald.malcles@umontpellier.fr)

Abstract. Elevated Plio-Pleistocene coastal and marine markers in stable continental regions are commonly explained
10   by a combination of eustatic sea-level variations and regional geodynamics (e.g., mantle dynamics, active faults). In this
study, we test the role of erosion rates on the Late Pleistocene uplift and landform evolution of the Armorican Massif,
western France. Denudation rates are estimated for 19 drainage basins using terrestrial cosmogenic nuclide (^{10}Be)
measurements in quartz. They range between 3 and 34 m.Ma^{-1}, with a factor of two difference between the western
highland region and the central lowland region (16 ± 8 m.Ma^{-1} vs. 9 ± 6 m.Ma^{-1}). Assuming a thin elastic plate model,
15   the lithosphere flexural isostatic response to these denudation rates produces an overall uplift of the Armorican
Peninsula from $12 – 15$ m.Ma^{-1} in the central lowland region to $4 – 10$ m.Ma^{-1} in the western peninsula and along the
coastline. We show that these erosion-driven uplift rates can explain the uplifted Late Pleistocene marine terraces along
the Armorican Peninsula coastline as well as the elevated Quaternary marine deposits in the central lowland region,
without necessitating additional geodynamic processes such as regional compression or local active faults. Our results
20   suggest that, in stable continental regions, long-term erosion should be taken into account as a driver of uplift and
deformation before trying to derive global or regional geodynamic or tectonic conclusions.

1. Introduction

Plio-Pleistocene uplift rates ca. $10 – 100$ m·Ma^{-1} are observed in numerous stable continental regions, i.e., in
25   areas unaffected by ongoing or recent tectonics (e.g., Australia, South Africa, northwestern Europe). Most of these uplift
rates are derived from elevated coastal landforms, such as marine terraces or planation surfaces (rasas), and from coastal
deposits, such as raised beaches. The origins of these slow coastal uplift rates have been attributed to a large variety of
geodynamic processes: global mantle dynamics (Gurnis et al., 2000) or plate tectonics (Pedoja et al., 2011), regional
lower crustal flow triggered by glaciation cycles (Westaway et al., 2002), local fault reactivation (Bonnet et al., 2000),
30   or local volcanism (Murray-Wallace et al., 1996). Surprisingly, none of these studies consider the role of long-term
erosion as a potential driver of coastal uplift through simple isostatic adjustment.

Here, we address the relationship between long-term erosion rates, uplift rates, and landform evolution of the
Armorican Massif, western France (Fig. 1) during the Late Pleistocene – Holocene period. This region comprises
several coastal landforms and marine deposits that witness recent upheaval of the whole area, including indications of
35   spatial variations that may reflect local fault reactivation (cf. Section 2). In addition to numerous uplift rate data, the
Armorican Massif also offers several specific advantages for testing the role of erosion in local and regional uplift: Due
to its peculiar geography, it is only affected by local erosion, with a negligeable impact of the surrounding erosion or

sedimentation systems (cf. Section 4). The overall massif erosion pattern can be estimated by quantifying erosion rates at a spatial scale of a few tens of kilometers owing to the relatively small watersheds. Finally, its geology consists

40   primarily of quartz-rich basement and metasediment formations, which allow for estimations of denudation rates at the scale of drainage basins using terrestrial cosmogenic nuclide (^{10}Be) measurements in quartz.
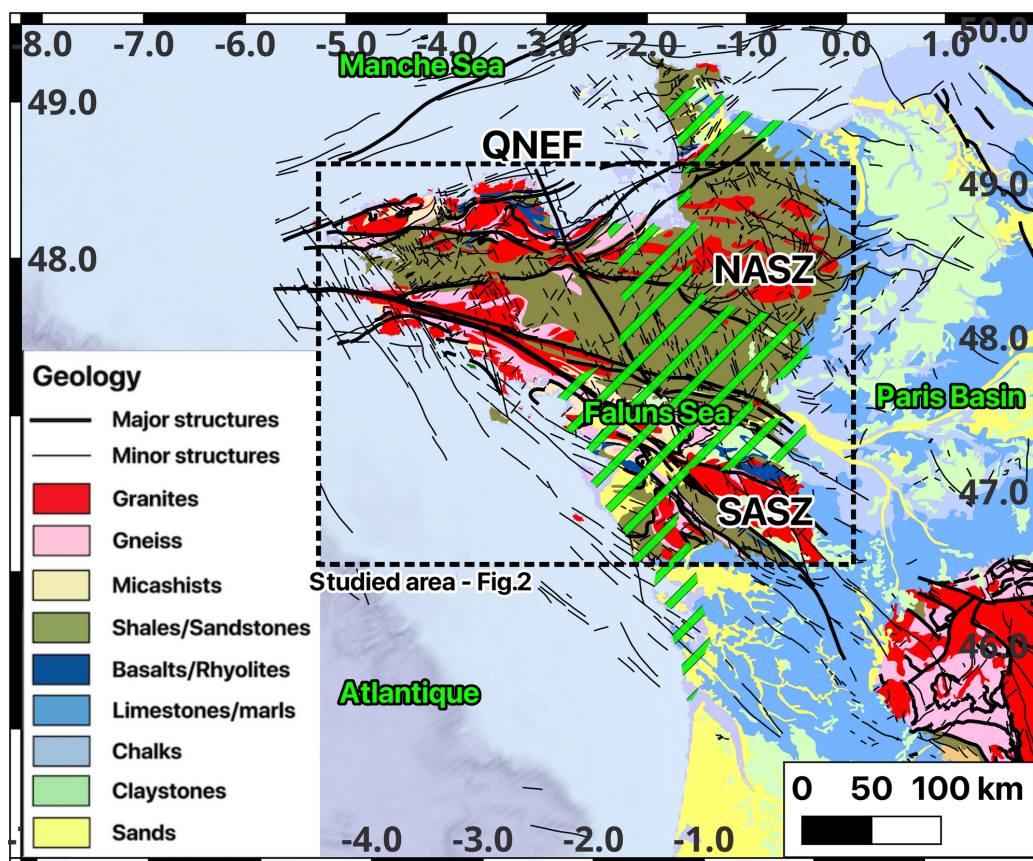
Figure 1: Armorican Massif context and simplified geology. Geological map (BRGM, 2023). Main tectonic structures shown in black (SASZ: South Armorican Shear Zone; NANZ: North Armorican Shear Zone; QNEF: Quessoy-Nort-sur-Erdre Fault). Blue stripes: approximate onshore extent of the Mio-Pliocene "Faluns Sea" (Néraudeau et al., 2010).

45

In the following, after a short description of the regional geological and geomorphological setting and evolution (Section 2), we detail the sampling strategy and processing methodology to derive new denudation rates in 19 watersheds covering the Armorican Massif (Section 3). These new data are then integrated within a regional Western Europe database to construct denudation rate models for the whole Armorican Massif and neighboring areas (Section 4),

50   which then serve as inputs for models of uplift rates driven by flexural isostatic adjustment (Section 5). Given the amplitudes and uncertainties in denudation rates, apparent uplift rates, and eustatic sea level corrections, our analyses show that Pleistocene – Holocene geological uplift rates in the Armorican Massif can be explained by the flexural isostatic response to local denudation rates, without need for additional processes such as lithosphere bulging or local fault activity. Additional processes cannot be ruled out but, if present, must be significantly slower than previously

55   proposed.

2. Geological and geomorphological setting

The Armorican Massif, western France, corresponds mostly to the remnant basement and structures of the Cadomian (650–540 Ma) and Variscan (370–300 Ma) orogens (Ballèvre et al., 2009). It comprises four main tectonic domains separated by major crustal-scale faults and shear zones (North-Armorican and South-Armorican Shear Zone systems, Nort-sur-Erdre Fault, Fig. 1). Its Meso-Cenozoic geological history is marked by minor fault reactivations associated with far-field tectonic events (e.g., North Atlantic Ocean opening, Pyrenean orogeny, …), up to the present-day moderate background seismicity indicating small ongoing deformation (Beucler et al., 2021). Overall, the Armorican Massif geology consists primarily of Proterozoic and Paleozoic crystalline basement and metasediment formations, with limited remnants of Meso-Cenozoic sedimentary deposits. Studies of planation surfaces indicate at least two major phases of burial and exhumation during the Mid Mesozoic and the Late Cretaceous – Early Eocene (Bessin et al., 2014). The thicknesses of the associated sedimentary covers (and thus the eroded thicknesses) are poorly constrained but were probably limited to several hundred meters, based on the remaining deposits. Several later episodes of minor marine transgressions and sediment deposits occurred during the Cenozoic, up to the most recent Red Sands and Faluns associated with the "Faluns Sea" (Fig. 1) during the Upper Miocene – Pliocene (Guillocheau et al., 2003).

These Red Sands and Faluns formations correspond to two cycles of marine transgressions / regressions during the Upper Miocene (5 – 8 Ma) and the Upper Pliocene (2 – 3 Ma), with marine flooding limited to the present-day low-elevation regions of central Brittany and Normandy (Fig. 1). While the Faluns deposits are characterized by shallow-depth open marine fauna, the Red Sands correspond to continental sheetflood, fluvial, and estuarine deposits (Néraudeau et al., 2003; Brault et al., 2004). Their sedimentary and stratigraphic characteristics point to a system of shallow-water marine transgressions between elevated continental domains, with an overall smooth topography and large braided rivers directly connected to numerous estuaries (Guillocheau et al., 2003; Brault et al., 2004). They also indicate a relatively high clastic discharge from two continental domains on both sides of main north-south divide (i.e., "West Armorican and North Cotentin islands" scenario). This Miocene – Pliocene configuration changes during the Mid Pleistocene (ca. 1 – 1.5 Ma), with the disappearance of marine deposits and the formation of the present-day drainage network that incises into the Red Sands and Faluns formations. In contrast with the Miocene – Pliocene system, the current (Pleistocene – Holocene) drainage network is characterized by incised valleys and jagged topography with a main east-west divide. The rivers tend to be spatially associated with tectonic scarps and structures, indicating either differential erosion along weaker inherited faults and shear zones, or a control by a potential recent reactivation of these structures (Bonnet et al., 1998, 2000).

The various Cenozoic marine deposits and landforms provide detailed information on the elevation history of different parts of the Armorican Massif. Hereafter, we refer to "apparent uplift" when considering the elevation of paleo marine markers relative the present-day sea level due to a combination of eustatic sea level variation and vertical land movement, in contrast with "uplift" which is used to refer to vertical land motion (i.e., corrected for eustatic variations).

The marine Miocene – Pliocene Faluns are found at present-day elevations between ca. 20 and 90 m. Assuming a eustatic sea level highstand of 60 m during the Upper Pliocene, (Brault et al., 2004) estimate an uplift of 12 – 40 m of the second maximum flooding surface situated in the central low-elevation region of the Armorican Massif. This would correspond to an average uplift rate in this area of 4 – 13 m·Ma^{-1} since ca. 3 Ma. This estimation is in rough agreement with those by (Bessin et al., 2017) based on a reanalysis marine deposits and sea-level curves, which yield average

Pleistocene uplift rates of 16 ± 2 and 29 ± 2 m·Ma⁻¹ for the low-elevation regions of Britany and Normandy. No uplift estimations exist for the high-elevation domains.

More recent estimations can be derived from the numerous Pleistocene marine terraces and rasas that mark the coastline of Brittany and Normandy. Using the compilation of (Pedoja et al., 2018), we estimate an average apparent uplift since MIS 5e (last interglacial, ca. 130 ka) of 6 m for western Brittany (31 terraces), 5 m for western Cotentin (7 terraces), and 8 m for the Channel Islands (4 terraces). These values are associated with an accuracy of 1 – 3 m based on the margin of error defined in (Pedoja et al., 2018) and on the data standard deviations. The eustatic sea level highstand during MIS 5e was located between ca. 3 m (Siddall et al., 2007) and ca. 7.5 m (Dutton and Lambeck, 2012) above present-day sea level, leading to an uplift between -1.5 m and 3 m for western Brittany, -2.5 m and 2 m for western Cotentin, and 0.5 m and 5 m for the Channel Islands (negative uplift values indicate subsidence). Thus, the Late Pleistocene may correspond to a period of slow uplift rate (15 – 40 m·Ma⁻¹) assuming a low eustatic highstand of 3 m, or a period of slow subsidence rate (-20 – 0 m·Ma⁻¹) for a high eustatic highstand of 7.5 m. For the penultimate interglacial (MIS 11, ca. 400 ka), (Pedoja et al., 2018) estimate an average apparent uplift of 20 m of western Europe marine terraces and rasas. Combined with a eustatic sea level highstand of 6 – 13 m (Muhs et al., 2012; Raymo and Mitrovica, 2012), this yields an average uplift rate of 18 – 35 m·Ma⁻¹ since 400 ka. We come back to these estimations in Section 6.

A few studies provide information on recent relative or absolute uplift rates in the Armorican Massif. Geomorphic analyses of river incisions and watershed morphologies indicate a differential uplift of ca. 30 m between western Britany (Oust watershed) and central Britany (Vilaine watershed) (Bonnet et al., 1998). A similar differential uplift of western Britany relative to the central low-elevation area is deduced from numerical analyses of the topography and slope / drainage relationships (Lague et al., 2000). Assuming a Pleistocene age of the current geomorphology, these studies indicate a relative west / center uplift rate of ca. 10 – 15 m·Ma⁻¹. (Bonnet et al., 1998) propose a faster relative rate of 40 – 60 m·Ma⁻¹ based on archeological finds in one terrace on the northern coastline of the Oust watershed. The leveling data analysis of (Lenôtre et al., 1999) supports the relative west vs. center uplift, albeit at a differential rate of 1000 m·Ma⁻¹ (1 mm·a⁻¹) or more. Recent results using GNSS (Global Navigation Satellite System) data show that this differential rate is likely overestimated, due to biases inherent to old leveling data, and that present-day vertical rates in the Armorican Massif are below the resolution of geodetic data, i.e., lower than ca. 500 m·Ma⁻¹ (0.5 mm·a⁻¹) (Masson et al., 2019).

3. Denudation rates from terrestrial cosmogenic nuclide

3.1. Drainage basin sampling and ¹⁰Be measurements

In order to estimate denudation rates at the scale of drainage basins, we sampled quartz-rich river sands (plus a few pebbles) and measured their concentrations of cosmogenic beryllium 10 (¹⁰Be), which is produced in quartz grains within the first few meters of the surface. This concentration is a function of the local surface production and denudation rates (Von Blanckenburg, 2005). Thus, ¹⁰Be measurements in river sands provide an estimation of the mean upstream denudation rate above the sampling point. We collected samples in exposed sand pockets along riverbanks and on sand bars, avoiding as much as possible accumulation spots due to anthropic structures and alterations of the river channel. This constraint, and the fact that downstream river sections close to the coast are often filled with mud, limited our sampling to upstream sites. In total, we sampled 19 watersheds (Table 1, Fig. 2), three of which were sampled twice

135   (a few meters apart) to estimate the repeatability between sand samples (Argenton, Layon, Leff). Three others were

sampled with both sands and cm-scale pebbles for comparison (Erdre, Douffine, Evel).
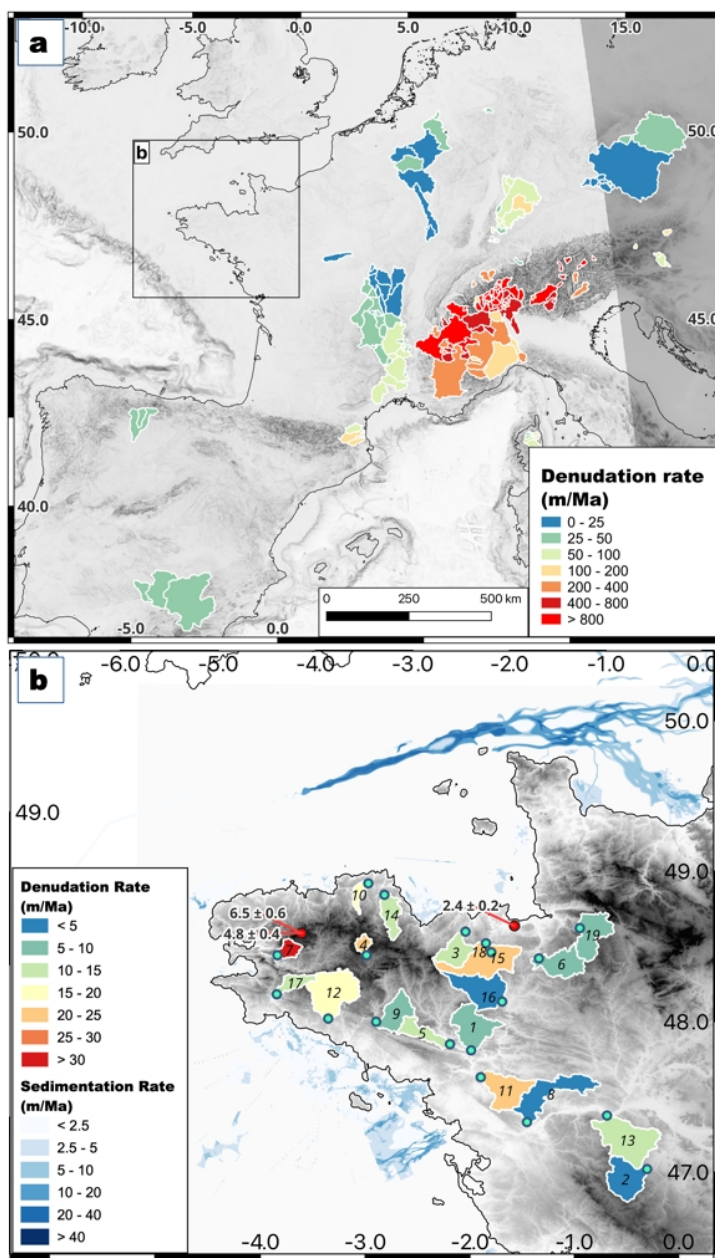
Figure 2. Drainage basin data used in the denudation rate model. A) Data from the Octopus drainage basin denudation database (Codilean et al., 2018) used for synthetic denudation rate modeling. B) Armorican Massif data from this study Blue dots: sampling locations of drainage basin, with basin number in each polygon (see table 1). Red dots: sampling locations of outcrops with estimated denudation rate. Quaternary sedimentation rates around the Armorican Peninsula from Augris et al. (2013c, a, b).

145   Sand and pebble samples followed a standard preparation procedure via crushing, sieving (retaining of the 250
– 1000 μm fraction), leaching with HCl + HNO$_3$ acids, magnetic separation, suppression of non-quartz grains using
multiple H$_2$SiF$_6$ baths, and final removal the atmospheric ^{10}Be by multiple HF etchings. From the purified quartz, Be
was separated following (Ruszkiczay-Rüdiger et al., 2021) via multiple ion exchange chromatography and selective pH
precipitation following total dissolution and the addition of 250 μL of known ^{9}Be concentration solution. After
150   separation, Be was oxidized at 800 °C and mixed with Nb (volumetric ratio ~ 1:1) prior to measurement. The ^{10}Be/^{9}Be
concentration ratio was measured by accelerator mass spectrometry at the ASTER national facility (Arnold et al., 2010).
The ratios were calibrated using ASTER standards (Braucher et al., 2015) to derive ^{10}Be concentrations.

        ^{10}Be concentrations in the three outcrop samples were measured following the same procedure. These three
155   sites (Fig. 2) are located at the top of locally prominent monadnocks (no topographic mask) and are therefore expected
to provide lower-bound erosion rates (i.e., rates mostly controlled by local weathering processes, with little influence of
longer wavelength slope-dependent hillslope or fluvial processes).

3.2. Denudation rates

160   Drainage basin average denudation rates were derived from ^{10}Be concentrations using the online CRONUS-
Earth system (Balco et al., 2008) (https://hess.ess.washington.edu/). This commonly-used calculator comprises some
simplifications and assumptions that we consider reasonable given our study context: e.g., denudation rates are at
steady-state; river sediments do not have a complex history following first exposure (no significant burial in river
terraces); mean watershed slope and latitude are used for computation of the production rate scaling factor. Given the
165   regional morphology (small elevation span), the homogeneous climate, and the small size of the sampled watersheds,
we consider that adding more complexity in our denudation rate estimations (e.g., spatial and temporal evolution of the
tree cover) would result in unnecessary questions and uncertainties. The estimated denudation rates are given in Table 1.
        The denudation rates measured in the 19 drainage basins of the Armorican Massif vary between 3 and 34
m.Ma^{-1}, for an average rate of 13 ± 7 m.Ma^{-1} (mean ± standard deviation). Assuming a sea-level high-latitude ^{10}Be
170   production rate of 4.11 ± 0.19 at.g^{-1}.yr^{-1} and the Stone scaling scheme (Stone, 2000), these denudation rates are
associated with an integration time between ca. 20 kyr and 200 kyr (average 45 kyr) (Von Blanckenburg, 2005). Thus,
they are representative of the Late Pleistocene period but are also sensitive to the Late Pleistocene - Holocene climate
transition and its impact on denudation rates (e.g., Schaller et al., 2002). Because of the integration times, we consider
that our rates are mostly indicative of Late Pleistocene average conditions, with only the fastest denudation rates (> 30
175   m.Ma^{-1}) potentially biased by the Holocene climate warming.
        Individual measurement uncertainties are ca. 1 – 2 m.Ma^{-1}. For the three sand samples repeated on the same
spot, the denudation rates vary by 0.5 – 4.5 m.Ma^{-1}. Differences for the Layon and the Leff rivers are within the
uncertainties, while the Argenton site shows a 4.5 m.Ma^{-1} discrepancy, outside of the measurement uncertainties even at
the 99% confidence level. Among the possible explanations, contamination by anthropogenic activity and sediment of
180   artificial low concentrations cannot be excluded. In any case, the Argenton results remain within the general low erosion
rate pattern. The sand / pebble sample comparison for the Erdre, Douffine, and Evel yields larger differences of 3 – 20
m.Ma^{-1}, the largest differences being associated with a sand denudation rate with a large uncertainty (Douffine, σ_d = 6

m.Ma^{-1}). Differences in the sand / sand comparisons have no clear explanation and may simply reflect the internal variability of the erosion and sediment transport system. This justifies using large-scale database to filter out such variability when deriving erosion laws (cf. Section 4.1). Hereafter, the denudation rate used for sites with sand / sand or sand / pebble samples is the average of both measurements.

The three outcrops show an average erosion rate of 4.6 ± 0.8 m.Ma^{-1}, roughly a third of the average denudation rate measured in the watersheds. This low value agrees with the expected erosion behavior for ridges and residuals reliefs (e.g., Dirks et al., 2016) and provides a lower bound for the local long-term erosion rate.

Name	area (km²)	mean altitude (m)	mean slope (°)	HI	Mass Qz (g)	Total count	^{10}Be/^{9}Be (10^{-13})	C ± σ_c (10^5 atm.g^{-1})	d ± σ_d (m·Ma^{-1})
Watersheds									
(1) Aff	712	78	2.6	0.39	18.429	1008	1.14 ± 0.04	3.77 ± 0.15	9.5 ± 0.9
(2) Argenton	651	155	1.8	0.51	28.973	939	3.59 ± 0.13	7.77 ± 0.31	4.6 ± 0.4
(2) Argenton					29.852	542	2.00 ± 0.09	0.42 ± 0.22	9.1 ± 0.9
(3) Arguenon	416	98	2.5	0.28	18.535	131	7.68 ± 0.07	2.56 ± 0.26	14.7 ±1.9
(4) Blavet	112	254	2.8	0.67	31.654	224	1.14 ± 0.09	2.18 ± 0.18	20.2 ±2.3
(5) Claie	353	97	2.8	0.52	29.535	566	1.43 ± 0.06	3.03 ± 0.15	12.2 ±1.2
(6) Couesnon	558	113	2.3	0.41	29.669	594	1.95 ± 0.08	4.11 ± 0.20	9.0 ± 0.9
(7) Douffine	173	155	5.0	0.41	30.371	44	0.59 ± 0.09	1.23 ± 0.19	33.6 ±6.0
(7) Douffine (c)					29.465	382	1.47 ± 0.09	3.12 ± 0.21	12.5 ±1.3
(8) Erdre	829	44	1.7	0.42	33.466	1281	3.30 ± 0.10	9.32 ± 0.33	3.4 ± 0.3
(8) Erdre (c)					20.561	1421	1.70 ± 0.05	5.19 ± 0.18	6.5 ± 0.6
(9) Evel	473	105	2.6	0.51	21.101	184	0.89 ± 0.07	6.18 ± 0.22	5.7 ± 0.5
(9) Evel (c)					31.191	1283	4.62 ± 0.14	2.64 ± 0.21	14.3 ±1.6
(10) Guindy	129	82	1.8	0.25	18.734	289	0.59 ± 0.04	1.96 ± 0.13	19.3 ±2.0
(11) Isac	681	42	1.5	0.42	20.030	812	0.52 ± 0.02	1.59 ± 0.07	22.9 ±2.1
(12) Laita	935	152	3.3	0.47	17.256	162	0.59 ± 0.05	2.15 ± 0.18	18.6 ±2.2
(13) Layon	1057	93	1.7	0.39	29.610	436	1.61 ± 0.08	3.40 ± 0.19	10.7 ±1.1
(13) Layon					31.325	682	1.74 ± 0.07	3.51 ± 0.16	10.3 ±1.0
(14) Leff	345	114	1.9	0.39	20.072	1228	0.92 ± 0.03	2.82 ± 0.11	13.6 ±1.2
(14) Leff					17.809	1226	0.87 ± 0.03	3.04 ± 0.12	12.5 ±1.1
(15) Linon	306	67	1.8	0.32	34.370	909	3.20 ± 0.11	5.85 ± 0.24	5.8 ± 0.5
(16) Meu	764	90	1.9	0.34	17.852	1523	2.29 ± 0.07	7.84 ± 0.26	4.3 ± 0.4
(17) Odet	224	145	3.5	0.49	17.418	283	0.99 ± 0.06	3.44 ± 0.23	11.2 ±1.2
(18) Rance aval	894	87	2.0	0.27	24.13	481	0.66 ± 0.03	1.63 ± 0.09	23.5 ±2.3
(19) Selune	625	166	2.8	0.36	33.020	189	2.10 ± 0.16	3.95 ± 0.31	9.9 ± 1.1
Outcrops									
Mont Dol	-	56	-	-	26.659	2958	8.18 ± 0.14	19.27 ±00.2.55	2.4 ± 0.2
Roch'Tre-dudon	-	377	-	-	30.534	1255	4.25 ± 0.14	6.62 ± 00.6.20	6.5 ± 0.6
Roch'Tre-dudon	-	369	-	-	19.134	2041	2.04 ± 0.05	8.70 ± 00.4.34	4.8 ± 0.4

Table 1. Armorican Massif TCN denudation rates and morphology parameters. Name: Watershed or outcrop location name (Fig. 2). All watershed samples are river sand, unless marked (c) for cobbles. HI: hypsometric integral. Mass Qz : mass of dissolved quartz, weighted at 10^{-4} g precision. Total count is the number of count of ^{10}Be on the detectors. Provided ratio are blank corrected (mean of 5 blanks = 2.21 ± 0.52 E^{-15}. C and σ_c: ^{10}Be concentration and standard error. d and σ_d: denudation rate and standard error.

4. Regional models of denudation and sedimentation rates

In order to assess the amplitudes and spatial variations of uplift rates due to isostatic response to surface
200 unloading and loading processes, we construct a set of regional models of erosion and sedimentation rates that cover the
whole Armorican Massif and neighboring areas up to a few hundred kilometers.

4.1. Denudation rate models

In theory, denudation rates at the watershed scale (over 100 km^2) are controlled by a combination of the
205 drainage basin morphology (e.g., slope, curvature), its lithology (e.g., soil cover, bedrock nature), its hydrology and
dynamics (e.g., runoff, drainage migration), and its local climate (e.g., temperature, precipitation). Several global
studies have attempted to define relationships between measured denudation rates and various combinations of
explanatory parameters (Harrison, 2000; Summerfield and Hulton, 1994; Von Blanckenburg, 2005; Portenga and
Bierman, 2011; Harel et al., 2016; Codilean et al., 2018). While their application domains and their results vary, these
210 studies point out that any single parameter or multi-parameter combinations do not predict denudation rates better than
within a factor of roughly two or three. All studies also agree that the mean basin slope (or an equivalent proxy) is the
most powerful explanatory parameter. However, the relationship between denudation rates and mean slopes breaks
down for slope values above 25 – 30°, due to the non-linearity of sediment flux - slope relationship when slopes get
closer to stability threshold (Binnie et al., 2007; Montgomery and Brandon, 2002).

215

	Area	Elevation		Slope		HI	Area < 1°
		mean	σ	mean	σ		
Armorican Massif	-0.27	0.25	0.42	0.51	0.48	-0.06	-0.27
Octopus + AM	-0.23	0.82	0.72	0.76	0.75	0.40	-0.40

Table 2. Denudation rate correlations with basin morphology parameters : Correlation as Pearson coefficient of correlation. For elevation and slope, correlations are given for the mean and the standard deviation (σ) of the distribution. HI: hypsometric integral. Area < 1°: percentage of basin area with slope lower than 1°. Armorican massif: new data for the Armorican Massif alone. Octopus + AM: final dataset including filtered Octopus and Armorican massif data (cf. Text).

In order to build our regional denudation rate models, we analyze denudation rate data for drainage basins from
the Octopus database (Codilean et al., 2018) over the non-tectonic areas of Western Europe (Fig. 2). This database is
further filtered to exclude data considered not representative of our study's spatial and temporal scales: We exclude
225 denudation rates higher than 1500 m·Ma^{-1} (integration times smaller than a few hundred years), those associated with
watershed areas larger than 30,000 km^2 (integration surface too large for regional modeling), and those associated with
areas smaller than 100 km^2 (integration surface too sensitive to local transient processes). Our new data from the
Armorican Massif complete the Octopus data set by providing information for this up-to-now unsampled low-slope
region (Fig. 2 and 3). The final dataset comprises 220 denudation rates and morphology parameters, whose correlation
230 is indicated in Table 2. The mean basin slopes and mean basin elevations show the highest correlations with denudation
rates, in agreement with global studies. For the Armorican Massif data alone, the correlations are significantly lower,
especially for the mean elevation, due to the low spread of denudation rates and morphology parameters.
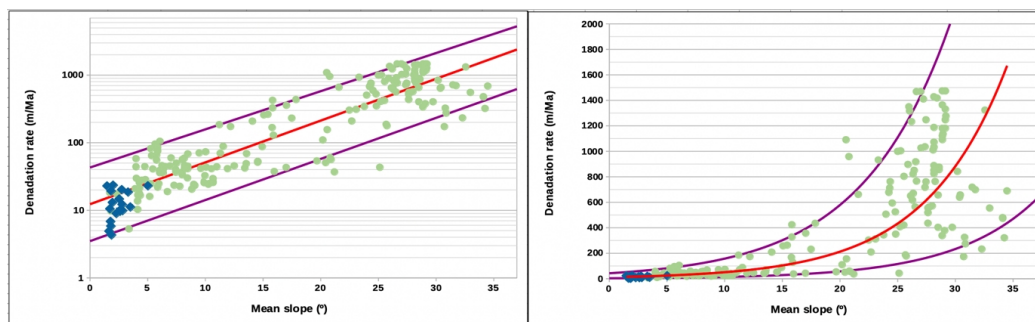
Figure 3: Model of denudation rates (m.Ma⁻¹) vs. mean basin slopes (°). The left and right panels are semi-log and linear representations. Green and blue symbols are from the Octopus database and this study. Best-fit and minimum/maximum exponential predicting functions are shown in red and purple lines (cf. Text).

Our complete regional erosion models are built using the mean slope parameter on a grid of hexagons with an area of 100 km² (roughly the minimal area of our Octopus + Armorican Massif database), i.e., a grid node spacing of ca. 6 km. We do not attempt to fit a process-based relationship for the prediction of erosion; rather, we derive an empirical relationship to produce a continuous erosion map from our isolated observations. The relationship between mean slope (s in °) and denudation rate (d in m·Ma⁻¹) is based on an exponential function in order to account for the nonlinearity for slope - denudation relation (Fig. 3). The best-fit function ($d = 12.3\ exp(0.142\ s)$) is associated with a root-mean-square (RMS) misfit of 22 m·Ma⁻¹, strongly controlled by the high denudation rate values (Fig. 3). For the Armorican Massif dataset alone ($s < 5°$), it yields a much smaller RMS misfit of 2 m·Ma⁻¹. In order to account for the variability of denudation rates for a given slope value, we estimate two upper- and lower-bound functions that comprise 90% of the data ($d_{max} = 43\ exp(0.130\ s)$ and $d_{min} = 3.5\ exp(0.140\ s)$). These two functions are adjusted manually to each exclude 5% of the data over the whole range of denudation rates (Fig. 3).

We use these functions to define two denudation rate models (Fig. 4):

- A mean model based on the best-fit function for all grid cells. Its denudation rates are strongly correlated with the topography and altitude on a regional scale (ca. 100 km), with relatively high rates ca. 15 – 25 m·Ma⁻¹ in the high-altitude zones of western Brittany and northeastern Brittany - southern Cotentin, and the lowest rates ca. 5 – 15 m·Ma⁻¹ in the low-altitude central region.
- A random model in which each grid cell is associated with a denudation rate based randomly on the lower-bound, best-fit, or upper-bound function. This alternative model will be used to test the sensibility and potential biases of the predicted uplift rates (cf. Section 5). This model results in an average denudation rate larger than that of the mean model by a factor of 1.6, due to the asymmetry of the upper- and lower-bound functions relative to the best-fit one (i.e., the average of the d_{min} and d_{max} functions is 1.5 times larger than the best-fit function for the whole slope range). The random model is not correlated with topography and comprises areas of concentrations of high (50 – 70 m.Ma⁻¹) and low (3 – 7 m.Ma⁻¹) denudation rates over distances of 30 – 50 km interspersed between a smaller wavelength (ca. 10 km) random distribution.
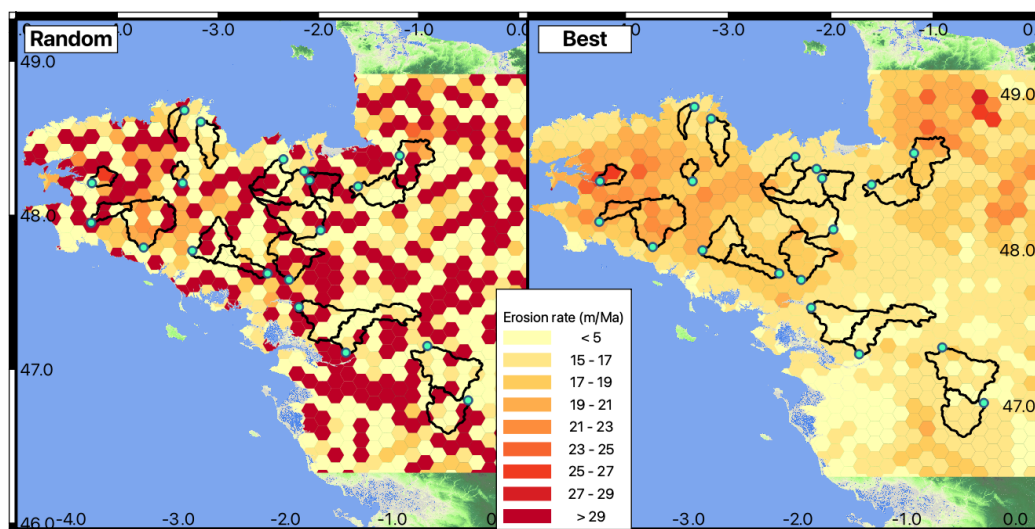
265 **Figure 4: Best-fit and random denudation rate models. Denudation rates modeled on 100 km² hexagons (6-km grid spacing) using the best-fit (right) and random (left) predictions models (cf. text). Sampled drainage basins and sampling locations are shown by the black outlines and blue dots.**

4.2. Sedimentation rates

270   The Pleistocene – Holocene offshore sedimentation around the Armorican Massif is characterized by two main phases: (1) near-field sedimentation along the present-day coastline during the sea-level highstands (interglacial periods) and (2) far-field sedimentation on the continental slope and rise during the sea-level lowstands (glacial periods).

The first phase corresponds to limited terrigenous sedimentation on the continental shelf, primarily at the outlet
275   of the local rivers. Sediment types and thicknesses have been mapped using a marine geophysical and coring surveys (Augris et al., 2013c, a, b), indicating a Quaternary cover of a few meters, up to a few tens of meters in some very localized pockets at the main river mouths (Fig. 2). The English Channel (Manche) is a clear exception to this general pattern, with Quaternary sediment thicknesses up to ca. 50 m localized in the channel of the paleo Fleuve Manche river. These deposits are not dated but are assumed to be the accumulation of Quaternary highstand sedimentation owing to
280   their geological and geophysical signature (L. Simplet, pers. comm.). Thus, the 1 – 5 m sediment thicknesses correspond to an average sedimentation rate of ca. 0.5 – 2.5 m·Ma⁻¹ over the last 2.5 Ma, with peaks up to 10 – 20 m·Ma⁻¹ in the localized high-sedimentation zones. These sedimentation rates are either too low (one order of magnitude smaller than land denudation rates) or too localized to produce significant effects on land (subsidence rates of 0 – 2 m·Ma⁻¹, Fig. 5).

285   The second phase of sedimentation corresponds to large deposits on the continental slope and rise and the oceanic basin during the Pleistocene lowstands. These large turbidite deposits correspond to the combined discharge of the main northwestern Europe rivers through the "River Manche" during the glaciation periods (Toucanne et al., 2009, 2010). The average sedimentation rates may reach a few tens of m·Ma⁻¹ at distances of 150 – 250 km from the Armorican Peninsula.

290   Based on a simple 2D model, we estimate that these sedimentation systems can generate uplift rates ca. 0.5 – 1 m·Ma⁻¹ on land, about ten times smaller than the effect of denudation rates (Fig. 5). Due to the low effects of the

sedimentation rates on land vertical motions and to the sparse distribution of sediment thickness mapping, we do not include the sedimentation rates in the following models (Section 5). This leads to a small overestimation of ca. 5 – 15 % of the uplift rates along the coastline and less than 5% further inland (cf. Fig. 5). This effect should be kept in mind

295   when discussing specific model predictions along the coastline.
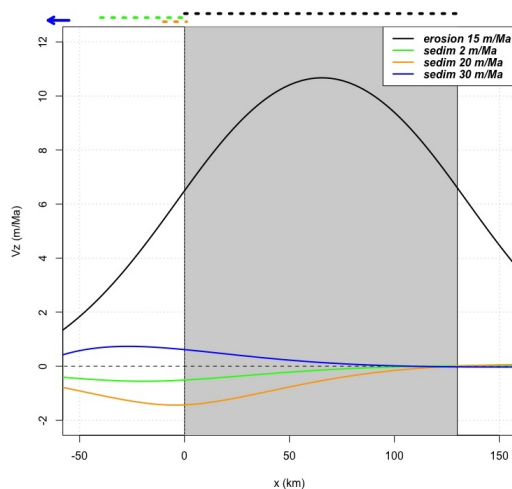
Figure 5: Schematic 2D models of uplift rates due to on-land erosion rates and offshore sedimentation rates. Uplift rates (Vz) shown as a function of distance (x) along a schematic 2D South-North profile across the Armorican Peninsula, with the gray area indicating the land section. The black curve shows uplift rates due on-land erosion rate of 15 m.Ma⁻¹ (0 ≤ x ≤ 125 km).

300   **The green, orange, and blue curves show uplift rates due to three sedimentation rate scenarios: 2 m.Ma⁻¹ on a 40 km-wide coastal section (-40 ≤ x ≤ 0 km), 20 m.Ma⁻¹ on a 10 km-wide coastal section (-10 ≤ x ≤ 0 km), 30 m.Ma⁻¹ on a 100 km-wide continental slope section (-270 ≤ x ≤ -170 km). Uplift rates are given for an elastic plate thickness of 25 km (cf. Section 5). Dashed lines above the graph show locations of the erosion / sedimentation zones.**

305   **5. Erosion-driven uplift rates**

The mechanical response of the lithosphere to surface erosion can be modeled with different assumptions, depending primarily on the time scale of erosion. For short erosion pulses (days to years), the response can be assumed to follow that of a semi-infinite elastic body (Steer et al., 2014). At the other end of the spectrum, standard Airy or Pratt isostatic response can be considered over very long time scales of tens of million years (Haxby and Turcotte, 1976). For

310   intermediate time scales of thousands of years to million years, the response to erosion is commonly modeled using a thin elastic plate overlying a low-viscosity fluid (Champagnac et al., 2007; Stephenson and Lambeck, 1985) or using more complex elasto-visco-plastic rheologies (Vernant et al., 2013; Mazzotti et al., 2023). For domains with standard or low continental geotherm or strong rheology, the response of an elasto-visco-plastic lithosphere is close to that of an elastic plate, whereas it may differ significantly in domains with high geotherm or weak rheology (Mazzotti et al.,

315   2023).

Here we model the vertical deformation due to Late Pleistocene – Holocene erosion rates following the common assumption of an elastic plate, representing the flexural rigidity of the lithosphere. We use the 3D model gFlex (Wickert, 2016) to produce maps of vertical velocities for our two denudation rate models coupled with a range of elastic plate thicknesses derived from rheology and from gravity-topography coherence analyses over Western Europe

320   (Tesauro et al., 2009; Kaban et al., 2018). For the Armorican Massif and neighboring regions, these studies indicate

elastic plate thicknesses varying between ca. 15 – 20 km and ca. 35 – 40 km. Lateral variations are poorly constrained and show either an eastward increase (Kaban et al., 2018) or small decrease (Tesauro et al., 2009). Thus, we test three cases of uniform elastic thicknesses of 15, 25, and 35 km to cover the observed range. Additional model parameters include the plate elastic rigidity (10 GPa) and Poisson ratio (0.25), and the crust and mantle densities (2700 and 3200 kg.m³, respectively). The spatial extent of our denudation rate models (Fig. 4) is limited to the north by the Cotentin Peninsula (not included) and to the east and south by the presence of the Paris and Aquitaine sedimentary basins (not included). Based on the response pattern of a 25-km-thick elastic plate (Fig. 5), we consider that the predicted uplift rates are valid up to ca. 50 km of the model eastern border and are thus limited to the Armorican Peninsula and the central Brittany lowland.
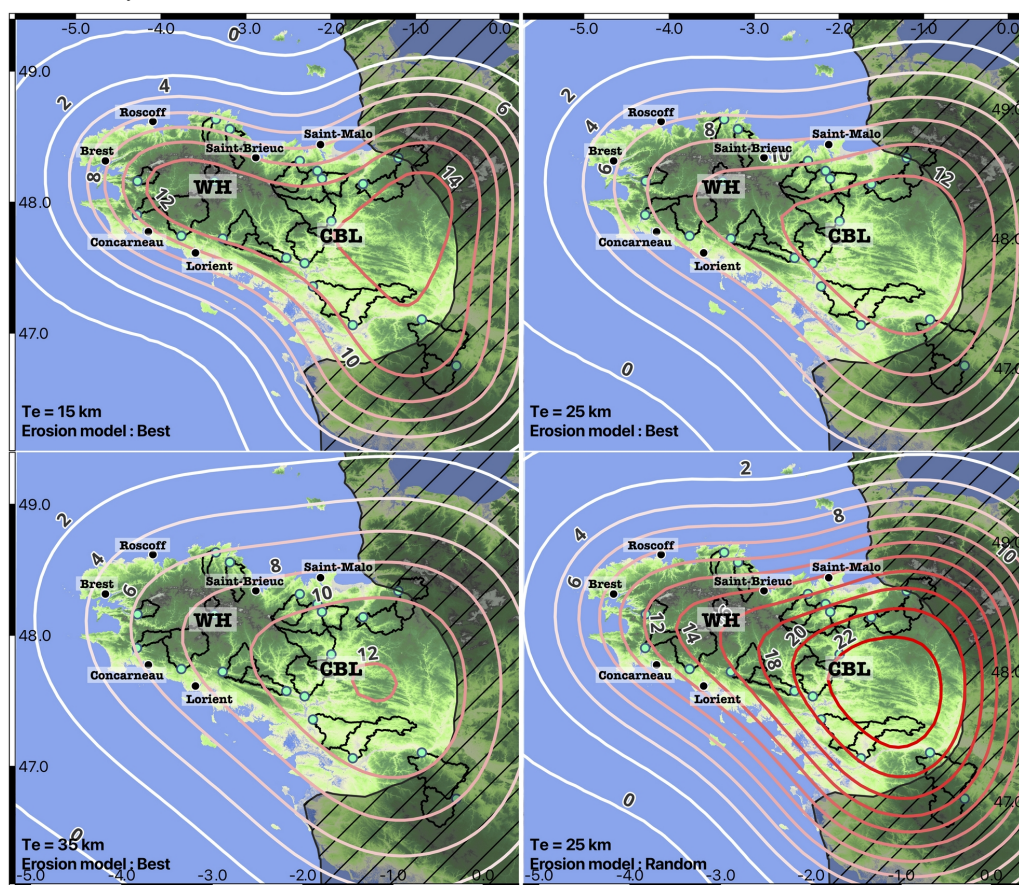
Figure 6: Predicted Late Pleistocene – Holocene uplift rates due to denudation rates. Isocontours of uplift rates in m.Ma⁻¹. A, B, C: Best-fit erosion model and three elastic plate thicknesses (15, 25, 35 km). D: Random erosion model and 25 km elastic plate thickness. The grey dashed area on the east side shows where uplift rates are biased by model border effects and must not to be considered. CBL and WH stands for Central Britanny Lowalnd and Western Highland respectively.

Figure 6 (A, B, C) shows the uplift rates predicted for the mean denudation rate model associated with the three elastic thickness cases. All three models show maximum uplift rates ca. 12 – 15 m.Ma⁻¹ centered on the central Brittany lowland. The uplift rates decrease westward down to 4 – 10 m.Ma⁻¹ in the Armorican Peninsula, with a decrease gradient controlled by the elastic plate thickness (lower gradient for thicker plate). This pattern is simply

explained by the fact that uplift rates in central Brittany are due to the combined effects of erosion rates in all directions,
whereas uplift rates in the Armorican Peninsula are only due to erosion rates in the peninsula itself, thus producing a
smaller combined effect. Uplift rates along the Armorican Peninsula coastline are ca. 8 m.Ma^{-1} in the northeast (Saint-
Malo, Saint-Brieuc) and southeast (Lorient, Saint-Nazaire) regions. They diminish to $4 – 6$ m.Ma^{-1} along the western tip
of the peninsula (Roscoff, Brest, Concarneau). The smallest plate-thickness model (Te = 15 km) shows a characteristic
elongated pattern of uplift rate ca. $10 – 13$ m.Ma^{-1} along the peninsula east-west axis. This pattern progressively
disappears in the thicker plate models (Te = 25 km and Te = 35 km) due to the low-pass filtering effect of the elastic
plate response that smooths out the erosion rate spatial distribution.

The random model allows us to test two effects: (1) the sensibility of the predicted uplift rates to the spatial
distribution of denudation rates, and (2) the possible bias of uplift rates due to the nonlinear slope-denudation rate
relationship. Figure 6D shows an example of uplift rates associated with a random denudation rate distribution (Fig. 4A)
for a Te = 25 km plate. The uplift rate pattern is similar in shape to that of the mean model, albeit with rates ca. $1.5 – 1.7$
times larger depending on the locations along the peninsula (Fig. 6) due to the denudation rates being on average 1.6
times larger than those of the mean model (cf. Section 4). This model illustrates two important points:

- Spatial variations in denudation rates over dimensions of $10 – 50$ km are filtered out by the flexural
  rigidity of the lithosphere and are not reflected in the uplift rates. This corresponds to a minimum
  sensitivity length that varies with the elastic plate thickness but in our case (Te = $15 – 35$ km) remains ca.
  50 km.
- Considering the uncertainties in denudation rates and the 90% envelop derived from our analysis of stable
  Western Europe data (Section 4), the random model results provide an upper bound for predicted uplift
  rates at any given point on the map (but not on average).

6. Discussion

6.1. Regional denudation and erosion rate variability

Despite the uncertainties on individual denudation rate estimations, we can rely on local and regional averages
to identify significant spatial variations. The main signal in the Armorican Massif is the difference between the western
highland and central lowland regions. The eight drainage basins fully or primarily eroding the western highland region
(Blavet, Claie, Douffine, Evel, Laita, Leff, Odet, and Guindy) show an average denudation rate of $16 ± 8$ m.Ma^{-1}. In
contrast, the nine basins eroding the central lowland (Aff, Argenton, Couesnon, Erdre, Isac, Layon, Linon, Meu, Selune)
show and average rate of $9 ± 6$ m.Ma^{-1}. Other potential geographic patterns (e.g., basins eroding the South Armorican
Shear Zone) cannot be identified. Although its statistical power is low, the difference of factor of 2 in denudation rates
between the western highlands and the central lowlands can easily be explained by the small difference in elevation and
in relief between the two areas. Quantitative morphological analyses of the topography indicate higher incision and
erosion by a factor of about $1.5 – 2$ in the western highland than in the central lowland (Bonnet et al., 1998; Lague et al.,
2000). The implications in terms of uplift derived in these studies are discussed in Section 6.2.

This west / center difference is also in agreement with the estimations of the mean annual sediment export of
rivers in these two areas (Delmas et al., 2012). The average export of rivers primarily associated with the western
highland is ca. 0.17 Mt.yr^{-1}, about twice as large as that of the Vilaine River located in the central lowland (ca. 0.07
Mt.yr^{-1}). Considering the respective areas of these two drainage systems, and assuming a sediment density of 1400
kg.m^{-3}, the equivalent erosion rates of the western and central regions are ca. 10 and 5 m.Ma^{-1}, about 60% of our

average denudation rates. Such a difference is commonly observed in studies comparing cosmogenic denudation rates
380 with sediment fluxes (e.g., Kirchner et al., 2001), due possibly to the different sampling time scales of the two methods
or to the fact that denudation rates sample both chemical and mechanical erosion processes while suspended sediment
flux data lack the dissolved load.

6.2. Late Pleistocene – Holocene uplift rates, regional sea level, and geodynamics

385 Based on present-day elevations of MIS 11 and MIS 5e marine terraces, (Pedoja et al., 2018) estimate mean
Middle Pleistocene and Upper Pleistocene apparent uplift rates of 50 ± 10 m.Ma^{-1} for most of Western Europe coastline,
including the Armorican Peninsula. Using morpho-stratigraphic evidence, they argue that these data cannot be
explained solely by eustatic sea-level variations and require a mean uplift rate of ca. 10 m.Ma^{-1}, at least for the Cotentin
Peninsula of western France, due to a "regional compression of the lithosphere".

390 Around the Armorican Peninsula, elevated marine terraces of MIS 5e age are found at an average elevation of
6 ± 2 m (full range 4 – 14 m). Glacial isostatic adjustment corrections and fingerprinting effects of past icesheets render
the estimation of regional Late Pleistocene sea levels particularly difficult (Hay et al., 2014). Relative to present-day sea
level, MIS 5e eustatic elevations are estimated ca. 2 – 9 m at 123 – 125 ka (with preferred value of 4.5 – 7.5 m) and ca.
-20 m at 113 ka, with a likely intermediate highstand ca. 5 m at 116 – 188 ka (Kopp et al., 2013; Polyak et al., 2018;
395 Hay et al., 2014). Thus, a potential regional eustatic sea level of 2, 4.5, 7.5, or 9 m results in a Late Pleistocene uplift
rate of -23, -12, 12, or 31 m.Ma^{-1} for the Armorican Peninsula marine terraces. In comparison, we estimate uplift rates
of 4 – 8 m.Ma^{-1} (upper bound of 6 – 14 m.Ma^{-1}) due to the response to denudation rates (Fig. 6).

Thus, within the uncertainties associated with the different sea level estimations, erosion-driven uplift can
explain the uplifted Upper Pleistocene marine terraces around the Armorican Peninsula, without a need for an additional
400 geodynamic process. Another way to consider these results is that, if denudation alone drives the uplift of the Armorican
Peninsula coastline, the elevation of the marine terraces constrains the regional Upper Pleistocene sea level to a
highstand ca. 5 m. A third interpretation is that additional uplift due to other geodynamic processes (in addition to
erosion) would require a low regional Upper Pleistocene eustatic sea level (2 – 5 m).

6.3. Quaternary morphology and tectonics
405
The elevations of marine deposits, corrected for past eustatic sea level, provide first-order estimations of
Quaternary uplift rates in the central lowland region of the Armorican Massif (Section 2). They indicate an average
uplift rate of 4 – 13 m·Ma^{-1} since ca. 3 Ma (Brault et al., 2004) or 16 ± 2 m·Ma^{-1} average during the Pleistocene (Bessin
et al., 2017). If we assume that our denudation rates are representative of the Quaternary period (mix of glacial and
410 interglacial periods), these geological uplift rates are in good agreement with those predicted in response to erosion (ca.
12 – 15 m.Ma^{-1}, upper bound ca. 20 m.Ma^{-1}, Fig. 6). As for the Upper Pleistocene marine terraces, this comparison
suggests that erosion-driven uplift is enough to explain the elevated Quaternary marine markers.

The pattern of uplift rates due to denudation rates also points out a minor difference between the western
highland (ca. 6 – 12 m.Ma^{-1}) and the central lowland (ca. 12 – 15 m/Ma^{-1}), depending on the assumed lithosphere
415 flexural rigidity (Fig. 6). Combined with the opposite pattern of best-fit denudation rates (ca. 20 and 15 m.Ma^{-1} in the
western and central regions, Fig. 4), these results suggest a quasi-stationary surface elevation in the central lowland
whereas the western highland region elevation diminishes by ca. 10 m.Ma^{-1}. These very low rates of evolution indicate a

persistence of the present-day elevation differences throughout the Quaternary, despite the Mid Pleistocene reconfiguration of the drainage network (Guillocheau et al., 2003; Brault et al., 2004).

420   Finally, our results do not support the proposed differential uplift rates across the Quessoy Fault accommodating 10 – 60 m.Ma^{-1} of east-side-down relative vertical motion (Bonnet et al., 1998). If erosion alone drives the Quaternary uplift, as suggested by the agreement with marine data, then the differential western / central uplift rates is less than a few m.Ma^{-1} and is in the opposite direction (east-side up). Additional processes (e.g., local tectonics) could induce additional uplift rates and result in the proposed relative Quessoy fault motion, but these would produce strong

425 uplift signals that are not recorded in the elevated marine terraces along the northern Armorican Peninsula coastline. A possible explanation for this conundrum is that the differential east-side-down signal proposed by (Bonnet et al., 1998; Lague et al., 2000) is only a difference in incision rates due to the slightly higher elevation of the western Armorican Peninsula.

430 **7. Conclusion**

       In the Armorican Massif, denudation rates measured from terrestrial cosmogenic nuclide concentrations range between 3 and 34 m.Ma^{-1}. These rates are representative of the Late Pleistocene (20 – 200 kyr). On average, the western highland region of the Armorican Massif shows denudation rates about twice those of the central lowland region (16 ± 8 m.Ma^{-1} vs. 9 ± 6 m.Ma^{-1}, Fig. 2 and 4B), in general agreement with previous regional morphology and erosion studies

435 (Bonnet et al., 1998; Lague et al., 2000; Delmas et al., 2012). There is no clear denudation signal associated with large-scale tectonic structures (e.g., South-Armorican Shear Zone).

       The lithosphere flexural isostatic response to these ongoing denudation rates results in an overall uplift of the Armorican Peninsula. Predicted uplift rates range from ca. 12 – 15 m.Ma^{-1} in the central lowland region to ca. 4 – 10 m.Ma^{-1} in the western peninsula and ca. 4 – 8 m.Ma^{-1} along the coastline (Fig. 6).

440   Considering the uncertainties in eustatic sea-level corrections, these erosion-driven uplift rates can explain the uplifted Late Pleistocene marine terraces along the Armorican Peninsula coastline (Pedoja et al., 2018), without necessitating additional geodynamic processes such as regional compression or local active faults. While our results do not preclude the existence of such other processes, they show that, if present, their effects must be much slower than previously proposed (Bonnet et al., 1998). Finally, assuming that they can be extrapolated over the whole Pleistocene

445 period, the erosion-driven uplift rates in the central lowland region are also sufficient to explain the elevated Quaternary marine deposits (Brault et al., 2004; Bessin et al., 2017).

       Our results show that long-term erosion over the Holocene and Pleistocene can be a major driver of the observed uplift in the Armorican Peninsula and, likely, in other stable continental regions. While other geodynamics processes may also contribute to these uplift rates, spatial variations in erosion rates should be taken into account for

450 before trying to derive global or regional geodynamic or tectonic conclusions (Gurnis et al., 2000; Pedoja et al., 2011; Murray-Wallace et al., 1996; Bonnet et al., 2000). They also suggest that the role of long-term erosion as a driver or promoter of intraplate seismicity should be considered in the Armorican Peninsula and other stable continental regions (Gallen and Thigpen, 2018; Mazzotti et al., 2023).

455 **Competing interests**

The contact author has declared that none of the authors has any competing interests

Acknowledgments

This study was supported by the French "Agence Nationale de la Recherche", project ANR-20-CE01-0005 "EroSeis".
460   Models, data analyses, and figures were done with open-source, free software (https://www.python.org/,
https://www.qgis.org/, https://github.com/awickert/gFlex). Model parameters and results are available on demand on the
Open Science Framework "EroSeis" project (https://osf.io/yq3bt/). We thank Laure Simplet (Ifremer) for providing the
sedimentation databases and information, and Samuel Toucanne (Ifremer) for the Fleuve Manche references.

465   **Bibliography**

Arnold, M., Merchel, S., Bourlès, D. L., Braucher, R., Benedetti, L., Finkel, R. C., Aumaître, G.,
Gottdang, A., and Klein, M.: The French accelerator mass spectrometry facility ASTER: Improved
performance and developments, Nucl. Instrum. Methods Phys. Res. Sect. B Beam Interact. Mater.
At., 268, 1954–1959, https://doi.org/10.1016/j.nimb.2010.02.107, 2010.

470   Augris, C., Simplet, L., and Gautier, E.: Isopaques de bancs sableux en Mer du Nord, Manche et Atlantique,
https://doi.org/10.12770/75AD486F-9D03-4FEB-B742-BE6C6F791345, 2013a.

Augris, C., Simplet, L., and Gautier, E.: Isopaques de couverture indifférenciée en Mer du Nord, Manche et Atlantique,
https://doi.org/10.12770/C841CA37-B414-4C51-AD6A-16BC34E8CF6F, 2013b.

Augris, C., Simplet, L., and Gautier, E.: Isopaques de nappes alluviales en Mer du Nord, Manche et Atlantique,
475   https://doi.org/10.12770/6C4CCD44-71B1-411D-91D1-ECCD1B2A46F1, 2013c.

Balco, G., Stone, J. O., Lifton, N. A., and Dunai, T. J.: A complete and easily accessible means of calculating surface
exposure ages or erosion rates from 10Be and 26Al measurements, Quat. Geochronol., 3, 174–195,
https://doi.org/10.1016/j.quageo.2007.12.001, 2008.

Ballèvre, M., Bosse, V., Ducassou, C., and Pitra, P.: Palaeozoic history of the Armorican Massif: Models for the tectonic
480   evolution of the suture zones, Comptes Rendus Geosci., 341, 174–201, https://doi.org/10.1016/j.crte.2008.11.009, 2009.

Bessin, P., Guillocheau, F., Robin, C., Schroëtter, J.-M., and Bauer, H.: Planation surfaces of the Armorican Massif
(western France):Denudation chronology of a Mesozoic land surface twice exhumed in response to relative crustal
movements between Iberia and Eurasia, Geomorphology, 233, 75–91, https://doi.org/10.1016/j.geomorph.2014.09.026,
2014.

485   Bessin, P., Guillocheau, F., Robin, C., Braun, J., Bauer, H., and Schroëtter, J.-M.: Quantification of vertical movement
of low elevation topography combining a new compilation of global sea-level curves and scattered marine deposits
(Armorican Massif, western France), Earth Planet. Sci. Lett., 470, 25–36, https://doi.org/10.1016/j.epsl.2017.04.018,
2017.

Beucler, É., Bonnin, M., Hourcade, C., Van Vliet-Lanoë, B., Perrin, C., Provost, L., Mocquet, A., Battaglia, J., Geoffroy,
490   L., Steer, P., Le Gall, B., Douchain, J.-M., Fligiel, D., Gernigon, P., Delouis, B., Perrot, J., Mazzotti, S., Mazet-Roux,
G., Lambotte, S., Grunberg, M., Vergne, J., Clément, C., Calais, É., Deverchère, J., Longuevergne, L., Duperret, A.,
Roques, C., Kaci, T., and Authemayou, C.: Characteristics and possible origins of the seismicity in northwestern France,
Comptes Rendus Géoscience, 353, 53–77, https://doi.org/10.5802/crgeos.86, 2021.

Binnie, S. A., Phillips, W. M., Summerfield, M. A., and Fifield, L. K.: Tectonic uplift, threshold hillslopes, and
495   denudation rates in a developing mountain range, Geology, 35, 743, https://doi.org/10.1130/G23641A.1, 2007.

Bonnet, S., Guillocheau, F., and Brun, J.-P.: Relative uplift measurement using river incisions: the case of the Armorican
basement (France), Comptes Rendus Académie Sci. - Earth Planet. Sci., 327, 245–251, 1998.

Bonnet, S., Guillocheau, F., Brun, J.-P., and Van Den Driessche, J.: Large-scale relief development related to Quaternary
tectonic uplift of a Proterozoic-Paleozoic basement: The Armorican Massif, NW France, J. Geophys. Res. Solid Earth,
500   105, 19273–19288, https://doi.org/10.1029/2000JB900142, 2000.

Braucher, R., Guillou, V., Bourlès, D. L., Arnold, M., Aumaître, G., Keddadouche, K., and Nottoli, E.: Preparation of ASTER in-house 10Be/9Be standard solutions, Nucl. Instrum. Methods Phys. Res. Sect. B Beam Interact. Mater. At., 361, 335–340, https://doi.org/10.1016/j.nimb.2015.06.012, 2015.

505 Brault, N., Bourquin, S., Guillocheau, F., Dabard, M.-P., Bonnet, S., Courville, P., Estéoule-Choux, J., and Stepanoff, F.: Mio–Pliocene to Pleistocene paleotopographic evolution of Brittany (France) from a sequence stratigraphic analysis: relative influence of tectonics and climate, Sediment. Geol., 163, 175–210, https://doi.org/10.1016/S0037-0738(03)00193-3, 2004.

Champagnac, J.-D., Molnar, P., Anderson, R. S., Sue, C., and Delacou, B.: Quaternary erosion-induced isostatic rebound in the western Alps, Geology, 35, 195–198, https://doi.org/10.1130/G23053A.1, 2007.

510 Codilean, A. T., Munack, H., Cohen, T. J., Saktura, W., Gray, A. G., and Mudd, S. M.: OCTOPUS: An open cosmogenic isotope and luminescence database, Earth Syst. Sci. Data, 10, 2123–2139, https://doi.org/10.5194/essd-10-2123-2018, 2018.

Delmas, M., Cerdan, O., Cheviron, B., Mouchel, J.-M., and Eyrolle, F.: Sediment export from French rivers to the sea, Earth Surf. Process. Landf., 37, 754–762, https://doi.org/10.1002/esp.3219, 2012.

515 Dirks, P. H. G. M., Placzek, C. J., Fink, D., Dosseto, A., and Roberts, E.: Using 10Be cosmogenic isotopes to estimate erosion rates and landscape changes during the Plio-Pleistocene in the Cradle of Humankind, South Africa, J. Hum. Evol., 96, 19–34, https://doi.org/10.1016/j.jhevol.2016.03.002, 2016.

Dutton, A. and Lambeck, K.: Ice Volume and Sea Level During the Last Interglacial, Science, 337, 216–219, https://doi.org/10.1126/science.1205749, 2012.

520 Gallen, S. F. and Thigpen, J. R.: Lithologic Controls on Focused Erosion and Intraplate Earthquakes in the Eastern Tennessee Seismic Zone, Geophys. Res. Lett., 45, 9569–9578, https://doi.org/10.1029/2018GL079157, 2018.

Guillocheau, F., Brault, Thomas, Barbarand, J., Bonnet, S., Bourquin, S., J, E.-C., Guennoc, P., Menier, D., Néraudeau, D., Proust, J.-N., and Wyns, R.: Histoire géologique du Massif Armoricain depuis 140 Ma (Crétacé-Actuel), Assoc. Géologues Bassin Paris, 40, 13–28, 2003.

525 Gurnis, M., Mitrovica, J. X., Ritsema, J., and van Heijst, H.-J.: Constraining mantle density structure using geological evidence of surface uplift rates: The case of the African Superplume, Geochem. Geophys. Geosystems, 1, n/a-n/a, https://doi.org/10.1029/1999GC000035, 2000.

Harel, M.-A., Mudd, S. M., and Attal, M.: Global analysis of the stream power law parameters based on worldwide 10Be denudation rates, Geomorphology, 268, 184–196, https://doi.org/10.1016/j.geomorph.2016.05.035, 2016.

530 Harrison, C. G. A.: What factors control mechanical erosion rates?, Int. J. Earth Sci., 88, 752–763, https://doi.org/10.1007/s005310050303, 2000.

Haxby, W. F. and Turcotte, D. L.: Stresses induced by the addition or removal of overburden and associated thermal effects, Geology, 4, 181, https://doi.org/10.1130/0091-7613, 1976.

Hay, C., Mitrovica, J. X., Gomez, N., Creveling, J. R., Austermann, J., and E. Kopp, R.: The sea-level fingerprints of 535 ice-sheet collapse during interglacial periods, Quat. Sci. Rev., 87, 60–69, https://doi.org/10.1016/j.quascirev.2013.12.022, 2014.

Kaban, M. K., Chen, B., Tesauro, M., Petrunin, A. G., El Khrepy, S., and Al-Arifi, N.: Reconsidering Effective Elastic Thickness Estimates by Incorporating the Effect of Sediments: A Case Study for Europe, Geophys. Res. Lett., 45, 9523–9532, https://doi.org/10.1029/2018GL079732, 2018.

540 Kirchner, J. W., Finkel, R. C., Riebe, C. S., Granger, D. E., Clayton, J. L., King, J. G., and Megahan, W. F.: Mountain erosion over 10 yr, 10 k.y., and 10 m.y. time scales, Geology, 29, 591, https://doi.org/10.1130/0091-7613(2001)029<0591:MEOYKY>2.0.CO;2, 2001.

Kopp, R. E., Simons, F. J., Mitrovica, J. X., Maloof, A. C., and Oppenheimer, M.: A probabilistic assessment of sea level variations within the last interglacial stage, Geophys. J. Int., 193, 711–716, https://doi.org/10.1093/gji/ggt029, 2013.

Lague, D., Davy, P., and Crave, A.: Estimating uplift rate and erodibility from the area-slope relationship: Examples from Brittany (France) and numerical modelling, Phys. Chem. Earth Part Solid Earth Geod., 25, 543–548, https://doi.org/10.1016/S1464-1895(00)00083-1, 2000.

Lenôtre, N., Thierry, P., Blanchin, R., and Brochard, G.: Current vertical movement demonstrated by comparative levelling in Brittany (northwestern France), Tectonophysics, 301, 333–344, 1999.

Masson, C., Mazzotti, S., Vernant, P., and Doerflinger, E.: Extracting small deformation beyond individual station precision from dense GNSS networks in France and Western Europe, Solid Earth, 10, 1905–1920, https://doi.org/10.5194/se-10-1905-2019, 2019.

Mazzotti, S., Vergeron, X., Malcles, O., Grosset, J., and Vernant, P.: Impact of long-term erosion on crustal stresses and seismicity in stable continental regions, Geology, 51, 733–737, https://doi.org/10.1130/G51327.1, 2023.

Montgomery, D. R. and Brandon, M. T.: Topographic controls on erosion rates in tectonically active mountain ranges, Earth Planet. Sci. Lett., 201, 481–489, https://doi.org/10.1016/S0012-821X(02)00725-2, 2002.

Muhs, D. R., Pandolfi, J. M., Simmons, K. R., and Schumann, R. R.: Sea-level history of past interglacial periods from uranium-series dating of corals, Curaçao, Leeward Antilles islands, Quat. Res., 78, 157–169, https://doi.org/10.1016/j.yqres.2012.05.008, 2012.

Murray-Wallace, C. M., Belperio, A. P., Cann, J. H., Huntley, D. J., and Prescott, J. R.: Late Quaternary uplift history, Mount Gambier Region, South Australia, Z. Geomorphol., Suppl.-Bd. 106, 41–56, 1996.

Néraudeau, D., Barbe, S., Mercier, D., and Roman, J.: Signatures paléoclimatiques des échinides du Néogène final atlantique à faciès redonien, Ann. Paléontol., 89, 153–170, https://doi.org/10.1016/S0753-3969(03)00023-5, 2003.

Pedoja, K., Husson, L., Regard, V., Cobbold, P. R., Ostanciaux, E., Johnson, M. E., Kershaw, S., Saillard, M., Martinod, J., Furgerot, L., Weill, P., and Delcaillau, B.: Relative sea-level fall since the last interglacial stage: Are coasts uplifting worldwide?, Earth-Sci. Rev., 108, 1–15, https://doi.org/10.1016/j.earscirev.2011.05.002, 2011.

Pedoja, K., Jara-Muñoz, J., De Gelder, G., Robertson, J., Meschis, M., Fernandez-Blanco, D., Nexer, M., Poprawski, Y., Dugué, O., Delcaillau, B., Bessin, P., Benabdelouahed, M., Authemayou, C., Husson, L., Regard, V., Menier, D., and Pinel, B.: Neogene-Quaternary slow coastal uplift of Western Europe through the perspective of sequences of strandlines from the Cotentin Peninsula (Normandy, France), Geomorphology, 303, 338–356, https://doi.org/10.1016/j.geomorph.2017.11.021, 2018.

Polyak, V. J., Onac, B. P., Fornós, J. J., Hay, C., Asmerom, Y., Dorale, J. A., Ginés, J., Tuccimei, P., and Ginés, A.: A highly resolved record of relative sea level in the western Mediterranean Sea during the last interglacial period, Nat. Geosci., 11, 860–864, https://doi.org/10.1038/s41561-018-0222-5, 2018.

Portenga, E. W. and Bierman, P. R.: Understanding Earth's eroding surface with 10Be, GSA Today, 21, 4–10, https://doi.org/10.1130/G111A.1, 2011.

Raymo, M. E. and Mitrovica, J. X.: Collapse of polar ice sheets during the stage 11 interglacial, Nature, 483, 453–456, https://doi.org/10.1038/nature10891, 2012.

Ruszkiczay-Rüdiger, Z., Neuhuber, S., Braucher, R., Lachner, J., Steier, P., Wieser, A., Braun, M., ASTER Team, Bourlès, D., Aumaître, G., and Keddadouche, K.: Comparison and performance of two cosmogenic nuclide sample preparation procedures of in situ produced 10Be and 26Al, J. Radioanal. Nucl. Chem., 329, 1523–1536, https://doi.org/10.1007/s10967-021-07916-4, 2021.

Schaller, M., Von Blanckenburg, F., Veldkamp, A., Tebbens, L. A., Hovius, N., and Kubik, P. W.: A 30 000 yr record of erosion rates from cosmogenic 10Be in Middle European river terraces, Earth Planet. Sci. Lett., 204, 307–320, https://doi.org/10.1016/S0012-821X(02)00951-2, 2002.

Siddall, M., Chappell, J., and Potter, E.-K.: Eustatic sea level during past interglacials, in: Developments in Quaternary Sciences, vol. 7, Elsevier, 75–92, https://doi.org/10.1016/S1571-0866(07)80032-7, 2007.

590 Steer, P., Simoes, M., Cattin, R., and Shyu, J. B. H.: Erosion influences the seismicity of active thrust faults, Nat. Commun., 5, 5564, https://doi.org/10.1038/ncomms6564, 2014.

Stephenson, R. and Lambeck, K.: Erosion-isostatic rebound models for uplift: an application to south-eastern Australia, Geophys. J. Int., 82, 31–55, https://doi.org/10.1111/j.1365-246X.1985.tb05127.x, 1985.

Stone, J. O.: Air pressure and cosmogenic isotope production, J. Geophys. Res. Solid Earth, 105, 23753–23759, https://doi.org/10.1029/2000JB900181, 2000.

595 Summerfield, M. A. and Hulton, N. J.: Natural controls of fluvial denudation rates in major world drainage basins, J. Geophys. Res. Solid Earth, 99, 13871–13883, https://doi.org/10.1029/94JB00715, 1994.

Tesauro, M., Kaban, M. K., and Cloetingh, S. A. P. L.: How rigid is Europe's lithosphere?, Geophys. Res. Lett., 36, https://doi.org/10.1029/2009GL039229, 2009.

Toucanne, S., Zaragosi, S., Bourillet, J. F., Cremer, M., Eynaud, F., Van Vliet-Lanoë, B., Penaud, A., Fontanier, C.,
600 Turon, J. L., and Cortijo, E.: Timing of massive 'Fleuve Manche' discharges over the last 350kyr: insights into the European ice-sheet oscillations and the European drainage network from MIS 10 to 2, Quat. Sci. Rev., 28, 1238–1256, https://doi.org/10.1016/j.quascirev.2009.01.006, 2009.

Toucanne, S., Zaragosi, S., Bourillet, J.-F., Marieu, V., Cremer, M., Kageyama, M., Van Vliet-Lanoë, B., Eynaud, F., Turon, J.-L., and Gibbard, P. L.: The first estimation of Fleuve Manche palaeoriver discharge during the last
605 deglaciation: Evidence for Fennoscandian ice sheet meltwater flow in the English Channel ca 20–18 ka ago, Earth Planet. Sci. Lett., 290, 459–473, https://doi.org/10.1016/j.epsl.2009.12.050, 2010.

Vernant, P., Hivert, F., Chéry, J., Steer, P., Cattin, R., and Rigo, A.: Erosion-induced isostatic rebound triggers extension in low convergent mountain ranges, Geology, 41, 467–470, https://doi.org/10.1130/G33942.1, 2013.

Von Blanckenburg, F.: The control mechanisms of erosion and weathering at basin scale from cosmogenic nuclides in
610 river sediment, Earth Planet. Sci. Lett., 237, 462–479, https://doi.org/10.1016/j.epsl.2005.06.030, 2005.

Westaway, R., Maddy, D., and Bridgland, D.: Flow in the lower continental crust as a mechanism for the Quaternary uplift of south-east England: constraints from the Thames terrace record, Quat. Sci. Rev., 21, 559–603, https://doi.org/10.1016/S0277-3791(01)00040-3, 2002.

Wickert, A. D.: Open-source modular solutions for flexural isostasy: gFlex v1.0, Geosci. Model Dev., 9, 997–1017,
615 https://doi.org/10.5194/gmd-9-997-2016, 2016.